River Research and Applications

WILEY

RESEARCH ARTICLE OPEN ACCESS

Addressing Unwanted Morphodynamic Processes in Re-Naturalization Projects

Lorenzo Durante[1] | Stefano Lanzoni[2] | Michele Bolla Pittaluga[1]

[1]Department of Civil, Chemical and Environmental Engineering, University of Genova, Genoa, Italy | [2]Department of Civil, Environmental and Architectural Engineering, University of Padua, Padua, Italy

Correspondence: Lorenzo Durante (lorenzo.durante@edu.unige.it)

Received: 19 May 2025 | **Revised:** 30 October 2025 | **Accepted:** 4 November 2025

Funding: This work was supported by the Autorità di Bacino Distrettuale del Fiume Po grant Updating the Po River Management Programme and integration with the delta branches (CUP D33C22001030001), by the Italian Ministerial grant PRIN 2022 Allogenic and Autogenic controls of DElta MOrphodynamics (AADEMO) (n. 2022P9Z7NP CUP D53D23004830006), and and by the Italian Ministerial PRIN PNRR 2022: Safety Equilibrium Conditions for rivers UndeR changing climatEs (SECURE) (n. P2022KA5CW CUP D53D23022870001).

Keywords: channel loops | river morphodynamics | river re-naturalization | sediment transport

ABSTRACT

River systems worldwide are undergoing severe ecological and morphological degradation due to prolonged anthropogenic interventions, such as channelization and dam construction, which disrupt sediment continuity and natural flow regimes. In response, river re-naturalization projects have emerged as essential strategies to restore the dynamics of fluvial systems. However, these actions frequently encounter unintended morphodynamic consequences, including sediment erosion and deposition, altered flow patterns, and disrupted channel stability, which pose significant challenges to achieving ecological, navigational, and flood management objectives. This study addresses the critical challenges associated with secondary channel re-opening, a common practice in re-naturalization projects, focusing specifically on lowland river systems. By employing a combination of numerical modeling and theoretical analysis, we investigate how key design parameters, such as localized levee lowering, influence the equilibrium of a river reach. The research highlights how an inappropriate project design can amplify sedimentation in the primary channel branch, reducing navigability, increasing maintenance costs, and offsetting ecological gains. To support management authorities and project designers, this work emphasizes the need for a multidisciplinary framework that incorporates long-term morphodynamic projections alongside ecological restoration goals. The findings provide insights into balancing environmental sustainability with operational functionality, offering guidance for improving the resilience and success of future re-naturalization efforts worldwide.

1 | Introduction

Globally, numerous rivers are currently in degraded conditions, exhibiting significant deterioration in both morphological and ecological aspects (Surian et al. 2009; Rinaldi et al. 2013). In highly anthropized regions, water quality has diminished, primarily due to the influx of fertilizers from agricultural activities, and wastewater from industrial and urban sources (Malmqvist and Rundle 2002; Vaughn 2010; Arthington et al. 2010). Additionally, the continuity of water flow and sediment transport is frequently disrupted by infrastructures, such as dams for hydropower and water intakes, which block the natural pathways of sediments and biota (Collas et al. 2018).

Historically, river channelization has been implemented to control natural river development and lateral migration, expand

land use, improve navigability and reduce flood risks (Simons et al. 2001). In recent years, there has been an emergence of river re-naturalization initiatives aiming to restore more natural river patterns and enhance ecosystem resilience. Common strategies in these projects include channel widening, reconstructing former channel shapes, and reconnecting the main channel with older side channels (Formann et al. 2007; Habersack and Piégay 2007; Poppe et al. 2016; Le et al. 2018). Such efforts have also been proposed for the Po River in northern Italy, a region heavily modified by human activities, with extensive agriculture and dense urban and industrial developments. Over the last century, the Po River was extensively channelized to manage its course and enhance navigability, often at the cost of isolating secondary channels through levee construction (Doriano and Sandra 1995; Marchetti 2002; Lanzoni et al. 2015; Rinaldi 2021).

Recent proposals aim to partially re-open these secondary channels, creating new morphological configurations that essentially consist of a bifurcation followed by a confluence. The re-opening of old cutoff channels aims at the recovery of the ecological corridor represented by the river bed and the natural perifluvial zone. This zone consists of remarkable bio-diverse habitats (gravel/sand beds, vegetated islands, sand banks, riparian vegetation, oxbow lakes, floodplain ponds) that are important for achieving the EU Biodiversity Strategy to 2030 (European Commission 2023). On the other hand, the re-designed bifurcation–confluence systems should ensure the maintaining of efficient flood risk protection and secure navigability conditions. The partial re-opening of secondary channels must then cope with two main aims, which can be in contrast with each other: enhancing biodiversity through re-establishing different habitats and ensuring hydraulic efficiency of the main river course. Indeed, bifurcation–confluence river units can lead to deposition/erosion processes also in the main channel, as extensively studied in idealized configurations (Bolla Pittaluga et al. 2003, 2015; Redolfi et al. 2019; Ragno et al. 2021; Durante et al. 2024). Typically, sedimentation occurs predominantly in the river branch with lower transport capacity, which can ultimately result in a complete avulsion favoring a single branch to dominate.

The present study considers a meandering river reach with a shorter, narrower cut-off channel that bypasses the longer meander bend. This configuration is quite common in the lowland portion of the Po River, as shown in Figure 1. Some insights into the potential evolution of this highly asymmetrical system can be obtained from simplified one-dimensional models in which the morphodynamics of bifurcations/confluences are parametrized through a physics-based two-cell model (Redolfi et al. 2019; Ragno et al. 2021; Durante et al. 2024). These models indicate that when the length differential between the main and secondary channel branches is sufficiently high the only possible solution is the one with the shorter branch becoming dominant. Despite providing clear and fast outcomes, this type of one-dimensional model assumes a simplified description of the two-dimensional flow and sediment exchange at the two-cell node (Bolla Pittaluga et al. 2003; Ikeda et al. 1981) and, therefore, provides approximate information in settings where lateral sediment transport is fully three-dimensional. Moreover, the re-opening of a side

FIGURE 1 | Example of the re-opening of an old cut-off channel adjacent to a meandering reach of the Po River, Italy, near Gussola, (Cremona, Italy) (44°58′N, 10°21′E). The re-activation of the secondary channel (depicted in violet) has been done by lowering the levee (denoted with a orange line) separating the main river bed from the old reach. This lowering allows part of the main river discharge to flow through the secondary channel. Flow is from left to right (*Source:* Google Earth). [Color figure can be viewed at wileyonlinelibrary.com]

channel through the localized lowering of the levee that separates it from the main river course usually produces a residual step at the entrance of this channel that could hinder sediment entering there. This would result in most sediments remaining in the main channel, potentially causing significant deposition in it.

This study systematically addresses the challenges associated with the re-opening of old cutoff channels through both reduced-complexity methods and comprehensive numerical simulations to deepen the understanding of the relevant morphodynamic processes. The paper is organized as follows. Section 2 provides a description of the system geometry (Section 2.1), and of the adopted one-dimensional (Section 2.2) and two-dimensional (Section 2.3) modeling approaches. The outcomes of both methods are reported in Section 3 with reference to two distinct configurations, characterized by different lengths of the main and secondary channels. Section 4, provides a comprehensive view of the potential impacts and dynamics of re-opening secondary channels in heavily modified rivers. Finally, Section 5 summarizes the conclusions of the research.

2 | Material and Methods

This study systematically addresses the design of levee lowering for the reactivation of secondary channel branches adjacent to the main course of the Po River. The reactivation is made through a side weir connecting the main channel with the inlet of the secondary channel (Figure 2). The height and length of this weir play a fundamental role in determining the amount of water and sediment diverted from the main channel into the secondary channel. This section first describes the system geometry, then presents the one-dimensional and two-dimensional formulations of the problem and, finally, delineates the design of the numerical simulations.

2.1 | System Geometry

The idealized framework used to analyze the effects of re-opening old cut-off channels consists of a meandering reach composed of three bends (denoted by suffixes as a, b, c, and d in Figure 2a), schematically reproducing the Po river stretch reported in Figure 1. The main channel is assumed to have a constant width $B_a = 200\,\mathrm{m}$ and an initially constant slope $S = 2 \times 10^{-4}$ (Figure 2b). The channel axis curvature has been approximated using the classical sine-generated curve (Leopold et al. 1964):

$$\theta = \theta_1 \sin(\lambda s), \tag{1}$$

where θ is the angle formed by the tangent to the channel axis with the valley direction, θ_1 is a parameter controlling the meander amplitude, s is the curvilinear longitudinal coordinate following the channel axis, and $\lambda = 2\pi / L_s$ is the intrinsic wave number of the meander. From this angular relationship, the curvature C of the meander axis is derived as:

$$C(s) = -\frac{d\theta}{ds}. \tag{2}$$

The secondary channel to be re-opened has a constant width B_c and a length L_c. It bifurcates from the main channel near the inflection point following the first meander bend apex (i.e., between s_1 and s_2), and rejoins the main channel in correspondence of the inflection point located after the second bend apex (i.e., between s_3 and s_4, Figure 2a). The initial slope of the secondary channel is determined by the elevation of the main channel at the bifurcation and confluence points. Both channel beds are assumed to be composed of uniform fine sediment with grain size $d_s = 0.5\,\mathrm{mm}$, while the channel banks are considered to be unerodible.

A weir is used to control the diverted flow (Figure 2b). This weir has a length equal to the width of the secondary channel (i.e., B_c), a top elevation h_W, and a height d with respect to the initial elevation of the main channel bed η_0. The height of the weir and the width of the secondary channel are crucial for the morphodynamic response of the bifurcation-confluence system. Two dimensionless design parameters are thus introduced, which relate the weir characteristics to the pre-intervention main channel geometry. They are the branch width ratio r_c, and the dimensionless inlet step parameter, $\widehat{d}$, defined as:

$$r_c = \frac{B_c}{B_a}, \qquad \widehat{d} = \frac{d}{D_a}, \tag{3}$$

where D_a represents the uniform flow depth of the main channel.

The morphodynamic equilibrium of the system depends also on the formative water and sediment discharges, Q_a and Q_{sa} flowing in the main channel. These discharges roughly correspond to those occurring at the stage for which the unvegetated sandy bars forming on the active portion of the river bed start to the flooded (Lanzoni et al. 2015). In the case of the Po river reach considered here, located approximately 40 km upstream of that investigated by (Lanzoni et al. 2015), the formative water discharge has been estimated to be approximately $Q_a = 1500\,\mathrm{m^3/s}$. The corresponding solid discharge at capacity, computed using the Engelund and Hansen (1967) total load formula, is $Q_{sa} = 0.158\,\mathrm{m^3/s}$. This value is consistent with that obtained from turbidity measurements at the gauge station of Polesine Parmense (PR), located about 12 km upstream of the locality shown in Figure 1. Note also that the value of the flow discharge corresponds to the threshold above which the side channel begin to be flooded in proposed design. The uniform flow depth associated with these formative conditions is $D_a = 5.6\,\mathrm{m}$. This estimate has been obtained by using the value of the Gauckler–Strickler coefficient typically used in the modeling of the considered Po River reach, $k_S = 30\,\mathrm{m^{1/3}/s}$.

Using these data, the width-to-depth ratio (β_a) and Shields parameter (ϑ_a) controlling the morphodynamics of main channel result:

$$\beta_a = \frac{B_a}{2D_a} = 17.8, \qquad \vartheta_a = \frac{q_a^2}{\chi_a^2 D_a^2 d_s \left(\rho_s - \rho\right)/\rho} = 1.358, \tag{4}$$

where $\chi_a = k_S D_a^{1/6}$ is the Chezy resistance coefficient, while ρ and ρ_s are the water and sediment density, respectively.

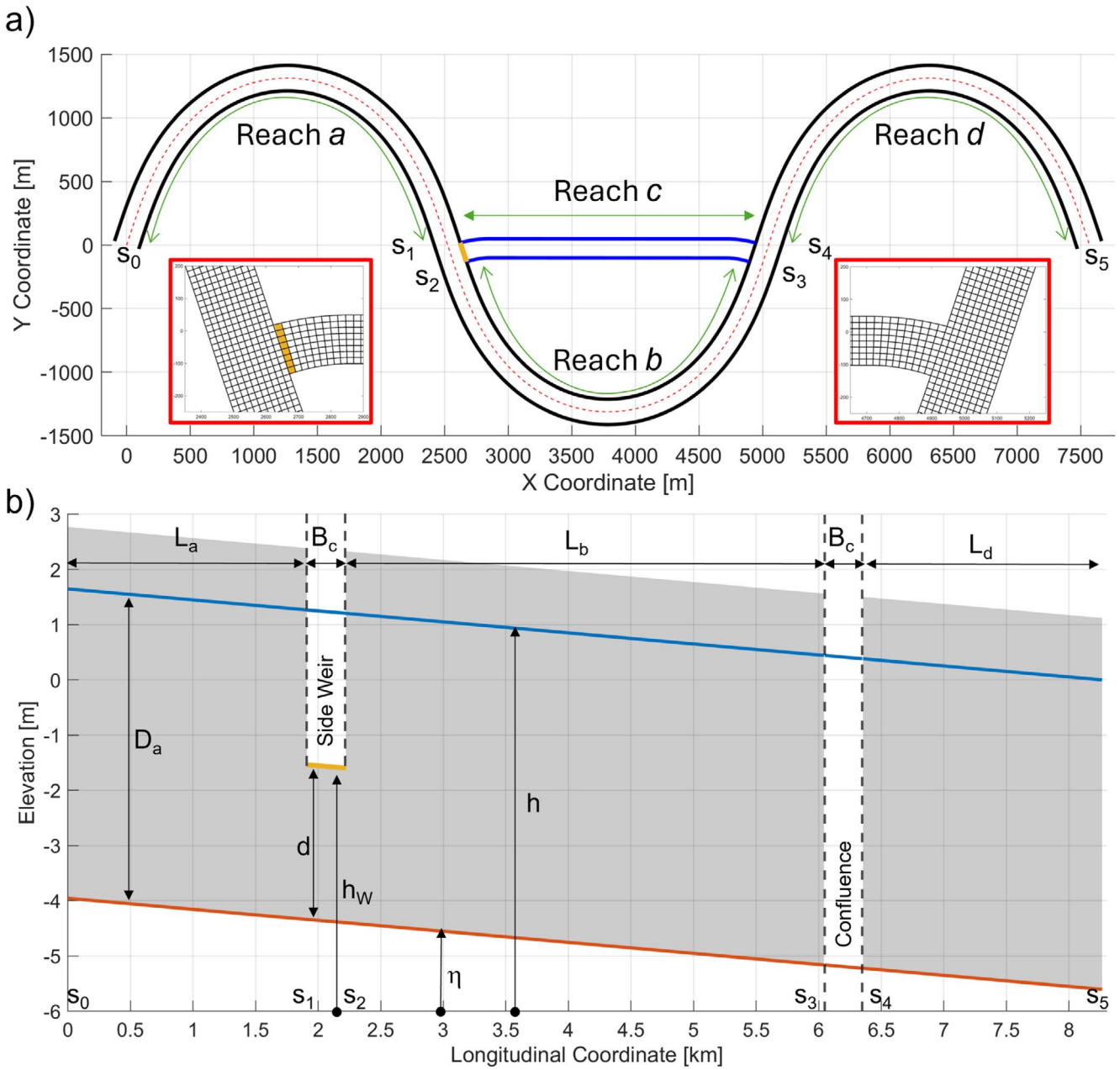

FIGURE 2 | (a) Planform view of the investigated river system. The banks and the axis of the main meandering channel are represented by black and red lines, respectively, while the secondary channel banks are depicted in blue. Inset maps illustrate the two-dimensional numerical grid at both the bifurcation and the confluence. (b) Longitudinal distribution of the mean bed elevation (orange line) and free-surface elevation (blue line) of the main channel in the initial equilibrium condition. The shaded gray region represents the extent of impermeable levees, while the vertical dashed lines indicate the locations of the bifurcation and confluence. The side weir at the bifurcation is depicted in orange. [Color figure can be viewed at wileyonlinelibrary.com]

Even though the dimensionless parameters (4) are also important for bifurcation-confluence dynamics (Bolla Pittaluga et al. 2003; Durante et al. 2024), in the present analysis they have been kept fixed and equal to the values characterizing the considered Po River reach. Conversely, the values of the branch width ratio and the inlet step parameters (3) have been varied to evaluate the effects of the reactivation of the secondary channel and provide information about the proper choice of the weir geometry.

2.2 | One-Dimensional Modeling

In a one-dimensional framework, the equilibrium bed profile of the meander bend illustrated in Figure 2 is computed considering the diversion of both water and sediment at the inlet of the cutoff channel, and reintegrating these quantities at the downstream confluence of the two branches. The cutoff channel is simply treated as a water and sediment bypass. The free surface and bed profiles within it are not computed, thereby neglecting

potential feedback mechanisms affecting the main meander course.

Under equilibrium conditions, provided that the boundary conditions, as well as the channel banks, do not vary in time, the one-dimensional equations ensuring the conservation of water, sediment, and the variation of momentum within a movable bed channel take the form (see, e.g., Seminara et al. 2024):

$$\frac{dQ}{ds} = \pm q_L, \tag{5a}$$

$$\frac{dQ_s}{ds} = \pm q_{sL}, \tag{5b}$$

$$\frac{dh}{ds} + \frac{Q^2}{gA}\frac{d}{ds}\left(\frac{1}{A}\right) = -\frac{Q^2}{\chi^2 A^2 R_h}. \tag{5c}$$

where Q and Q_s are the water and sediment discharges flowing through the channel, q_L and q_{sL} represent the lateral liquid and solid flow discharge per unit length which possibly leaves (minus sign) or enters (plus sign) the channel, h is the water surface elevation, A is the cross-sectional area, R_h is the corresponding hydraulic radius, g is the gravitational acceleration, and χ is the Chezy resistance coefficient. Assuming that the channel has a constant width B much larger than the mean flow depth D, the hydraulic radius can be approximated as $R_h \simeq D$. Moreover, the area becomes $A = BD$. The momentum equation can then be rewritten as:

$$\frac{d\mathscr{H}}{ds} = -J, \tag{6}$$

where $\mathscr{H}$ is the specific energy (i.e., per unit fluid weight), and J is the specific energy loss per unit length, defined as:

$$\mathscr{H} = h + \frac{Q^2}{2gB^2D^2}, \qquad J = \frac{Q^2}{\chi^2 B^2 D^3}. \tag{7}$$

At each cross-section, the local flow depth D is determined as that ensuring the sediment discharge at capacity corresponding to that section.

The equilibrium configuration of the channel bed is obtained by solving the three ordinary differential Equations (5a), (5b), and (6), complemented with suitable boundary conditions and auxiliary relationships for q_L and q_{sL}.

A constant flow discharge Q_a is imposed at the upstream boundary. The associated solid discharge Q_{sa} is assumed to be in equilibrium with the flow discharge. Given the fine character of the sediment, Q_{sa} is computed using the total load formula by Engelund and Hansen (1967). Moreover, Equation (6), is integrated numerically imposing the following condition at the downstream boundary:

$$\mathscr{H}|_{s=s_5} = \left[h + \frac{Q_a^2}{2gB_a^2D^2}\right]_{s=s_5}, \tag{8}$$

where h and D are the uniform flow values corresponding to Q_a.

The estimate of flow discharge diverted over side weirs has been extensively studied in the hydraulic literature (e.g., Paris et al. 2012; Michelazzo et al. 2016). Since head losses can be taken almost as negligible in lateral diversions, it is reasonable to assume that the specific energy of the flow at the weir remains constant (De Marchi 1934). Consequently, the flow discharge diverted laterally per unit length can be expressed as follows:

$$q_L = c_Q\sqrt{2g}D_W^{3/2}, \qquad s_1 \le s \le s_2, \tag{9}$$

where c_Q is the lateral discharge coefficient, set here at 0.4, and D_W represents the water depth above the weir. This latter quantity can be determined as the difference between the local free-surface elevation h and the weir elevation h_W:

$$D_W = h - h_W. \tag{10}$$

Accordingly, the total diverted flow discharge Q_c reads:

$$Q_c = \int_{s_1}^{s_2} q_L\, ds. \tag{11}$$

This discharge is subsequently linearly reintroduced downstream at the junction with the secondary channel, i.e., for $s_3 \le s \le s_4$:

$$q_L = \frac{Q_c}{B_c}, \qquad s_3 \le s \le s_4. \tag{12}$$

The modeling of the solid discharge diverted through the weir needs particular attention. Indeed, bedload is prevented from being diverted into the cutoff channel when the weir elevation h_W exceeds the local elevation of the main channel η. Thus, it is reasonable to assume that only the portion of the suspended load within the water column above the weir is diverted into the cutoff channel (Slingerland and Smith 1998).

Assuming, as a first approximation, that the average concentration $\overline{C} = Q_s/Q$ is in equilibrium with the local flow condition, the vertical distribution can be approximated using the classical Rouse profile. Considering the value of the Shield stress in front of the weir, depth-averaged concentration $\overline{C}$ is then computed as (see, e.g., Bolla Pittaluga and Seminara 2003, Seminara et al. 2024):

$$\overline{C} = \frac{c_a}{1-\zeta_a}\int_{\zeta_a}^{1}\left[\frac{(1-\zeta)}{\zeta}\frac{\zeta_a}{(1-\zeta_a)}\right]^Z d\zeta, \tag{13}$$

where c_a is the near-bed concentration, $\zeta = z/D$ is the vertical coordinate z normalized with the local flow depth D, ζ_a is the reference height typically set at 0.05, and $Z = w_s/ku_*$ is the Rouse number, with k the von Karman constant and u_* the shear velocity.

Only a portion the suspended sediment flowing in the main channel contributes to the sediment discharge entering the secondary channel, as illustrated in Figure 3a. To account for this,

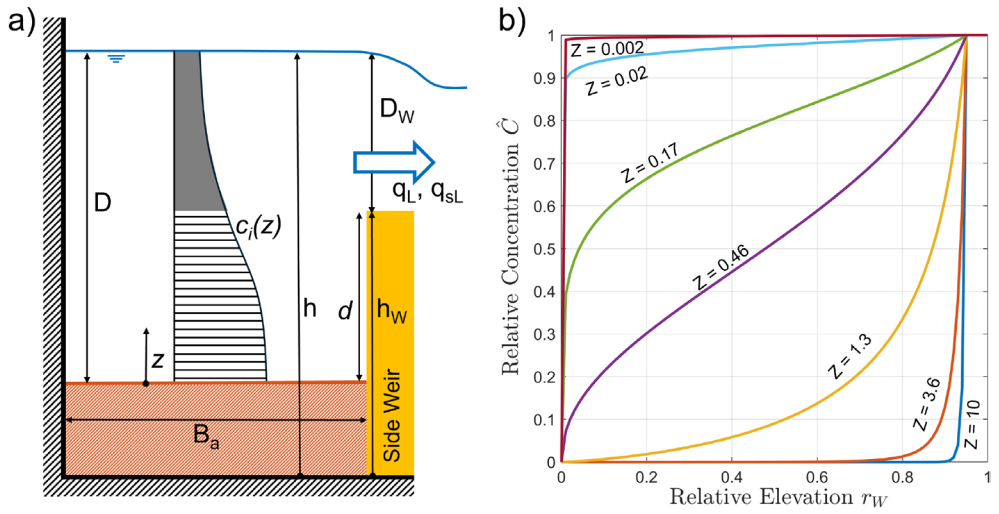

FIGURE 3 | (a) Schematic cross-section of the main channel at the location of a side weir, illustrating the vertical distribution of suspended sediment concentration $c_i(z)$ within the water column. The sketch highlights the portion of sediment potentially diverted into the cut-off channel through the side weir. (b) Relative depth-averaged concentration $\hat{C}$ as a function of relative elevation r_W above the weir crest, shown for various Rouse numbers Z. Each curve represents a different sediment transport condition governed by the value of Z. [Color figure can be viewed at wileyonlinelibrary.com]

we introduce the relative above-weir water depth r_W, defined as the ratio of the flow depth over the weir, $D_W = h - h_W$, to the main channel depth, $D = h - \eta$, namely:

$$r_W = \frac{D_W}{D}. \tag{14}$$

Note that this definition allows for the inclusion of cases where the initial weir elevation changes due to sediment deposition. Based on the relative weir depth, the depth-averaged concentration of suspended sediment diverted into the secondary channel through the weir can be computed as a percentage of the mean concentration in the main channel. This percentage coincides the relative depth-averaged concentration, $\hat{C}$, defined as:

$$\hat{C} = \frac{C_{div}}{\overline{C}} = \frac{(1-\zeta_a)}{(1-r_W)} \frac{\int_{r_W}^{1} \left[\frac{(1-\zeta)}{\zeta}\frac{\zeta_a}{(1-\zeta_a)}\right]^Z d\zeta}{\int_{\zeta_a}^{1} \left[\frac{(1-\zeta)}{\zeta}\frac{\zeta_a}{(1-\zeta_a)}\right]^Z d\zeta}. \tag{15}$$

The values are presented in Figure 3b for different values of the relative above-weir water depth. It clearly appears that $\hat{C}$ approaches 0 as r_W approaches 0 (i.e., $D_W = 0$). Conversely, higher values of relative above-weir depth imply that a greater fraction of suspended sediment is diverted in the secondary channel. Moreover, this fraction will increase for finer sediments (i.e., lower values of Z), and decrease for coarser sediments (i.e., higher values of Z) that tend to be transported closer to the bed.

Eventually, the diverted solid discharge per unit length (q_{sL}) is computed as:

$$q_{sL} = \overline{C}\hat{C}q_L, \qquad s_1 \le s \le s_2. \tag{16}$$

This relation holds until the weir elevation is above the elevation of the main channel bed. Conversely, when the weir is below the bed elevation, bedload is diverted into the secondary channel in addition to suspended load, and the diverted solid discharge needs to be computed as:

$$q_{sL} = q_L \frac{Q_s}{Q}, \qquad s_1 \le s \le s_2 \tag{17}$$

where Q and Q_s are the flow and sediment discharge, respectively, computed in the cross-section of the main channel immediately upstream of the bifurcation.

Analogously to the total diverted flow discharge Q_c, the total diverted sediment discharge Q_{sc} is calculated as:

$$Q_{sc} = \int_{s_1}^{s_2} q_{sL}\, ds. \tag{18}$$

The sediment discharge transported by the secondary channel is reintroduced at the downstream confluence with the main channel using the linear relation:

$$q_{sL} = \frac{Q_{sc}}{B_c}, \qquad s_3 \le s \le s_4. \tag{19}$$

The system of ordinary differential Equations (5a), (5b), and (6) is solved numerically starting from the downstream boundary ($s = s_5$). Here, h is determined based on Equation (8), taking into account that, under equilibrium conditions, the solid and liquid discharges must be equal to the upstream inputs (i.e., $Q_d = Q_a$ and $Q_{sd} = Q_{sa}$).

Noteworthy, as the computation arrives at the confluence, the lateral liquid and solid discharges are not known a priori. Consequently, an iterative procedure is employed to determine the appropriate combination of Q_b and Q_{sb} (and, accordingly, Q_c and Q_{sc}). The iterative process continues until the continuity constraints

$$Q_a = Q_b + Q_c, \qquad Qs_a = Q_{sb} + Q_{sc}, \tag{20}$$

are satisfied at both the bifurcation and the confluence.

The use of an iterative solution procedure is necessary due to the feedbacks between the flow field and the dynamics of the main channel bed. These feedbacks affect the free-surface elevation and the bed profile in the main channel reach between the bifurcation and the confluence (reach *b* in Figure 2a), as it will be discussed in detail below.

2.3 | Two-Dimensional Modeling

Although the one-dimensional approach introduced above can provide significant insights into the overall morphodynamic evolution of the meander-loop system investigated here, it gives only a rough description of the processes taking place at the bifurcation and at the confluence.

These localized phenomena and their evolution in time and space have thus been addressed through a systematic series of numerical simulations conducted using the numerical code Delft3D-Flow Flexible Mesh (https://www.deltares.nl/en/software-and-data/products/delft3d-fm-suite/modules/d-flow-flexible-mesh). This software is capable of performing multi-dimensional hydrodynamic simulations under non-stationary conditions, including also the bed evolution due to sediment transport, erosion, and deposition. The two-dimensional partial differential equations for the continuity and momentum of the liquid phase, and the conservation equation for the solid phase, are discretized using an implicit finite volume solver applied to a staggered, flexibly shaped grid. The boundary conditions associated to these equations are the water discharge and the corresponding equilibrium sediment discharge at the upstream section of the main channel, and a fixed free-surface elevation for uniform flow at the downstream section. In addition, given the fine character of the sediment composing the bed ($d_s = 0.5$ mm), the sediment transport intensity is again estimated using the total load formula proposed by Engelund and Hansen (1967).

The unstructured grid is designed to ensure an accurate representation of the localized processes under investigation. A minimum of 10 computational cells are thus employed in the transversal direction, maintaining a balance between resolution and computational cost. Secondary flow computation is activated in the model to accurately represent the flow structure along the meander bends and near the secondary channel inlet and outlet. Although the bifurcation-confluence areas present some three-dimensional features (Slingerland and Smith 1998; Michelazzo et al. 2016; De Ruijsscher et al. 2020; Lin et al. 2025), the two-dimensional approach adopted here effectively captures the overall morphodynamic trends near these areas, as well as the flow and sediment partitioning throughout the main and secondary branches. The presence of the weir at the inlet is modeled as a localized lowering of the main channel lateral levee, with the height based on the parameter $\widehat{d}$. To preserve the initial planform, the riverbed is treated as non-erodible in the cells corresponding to the side weir.

The morphodynamic equilibrium of both the main and secondary channel beds is analyzed by considering the same formative water and sediment discharges presented in Section 2.1 and, consequently, using the same values of the parameters β_a and ϑ_a appearing in relations (4). Conversely, the elevation of the side weir used to control the diverted flow, the width of the secondary channel and its length as compared to that of the main channel are varied by modifying the dimensionless parameters $\widehat{d}$ and r_c defined by the relations (3), and the parameters γ_L and Λ_b defined as (Durante et al. 2024):

$$\Lambda_b = \frac{L_b S}{D_a}, \qquad \gamma_L = \frac{L_c}{L_b}, \tag{21}$$

where L_b represents the length of the main channel branch from the bifurcation to the subsequent confluence, and L_c denotes the length of the cut-off channel. The numerical configurations investigated by varying the parameters Λ_b, γ_L, r_c, and $\widehat{d}$ are summarized in Table 1.

It is worthwhile to note that in one-dimensional modeling, the equilibrium configuration is determined by directly solving a system of ordinary differential equations. Conversely, in two-dimensional modeling, the morphodynamic evolution toward equilibrium is obtained through a time-marching approach. This approach involves solving a system of partial differential equations comprising the two-dimensional shallow water continuity and momentum equations, along with the two-dimensional

TABLE 1 | Characteristic dimensionless parameters representative of the numerical simulations conducted to determine the morphodynamic equilibrium of the main meander channel—secondary channel system illustrated in Figure 2.

ID	Λ_b	γ_L	r_c	$\widehat{d}$
Run 00	0.13	0.62	0.75	0.50
Run 01	0.13	0.62	0.75	0.75
Run 02	0.13	0.62	0.75	0.25
Run 03	0.13	0.62	0.75	0.00
Run 04	0.13	0.62	0.6	0.75
Run 05	0.13	0.62	0.6	0.5
Run 06	0.13	0.62	0.6	0.25
Run 07	0.13	0.62	0.4	0.75
Run 08	0.13	0.62	0.4	0.5
Run 09	0.13	0.62	0.4	0.25
Run 10	0.13	0.62	0.2	0.75
Run 11	0.13	0.62	0.2	0.5
Run 12	0.13	0.62	0.2	0.25
Run 13	0.16	0.82	0.4	0.25
Run 14	0.16	0.82	0.4	0.5
Run 15	0.16	0.82	0.4	0.75

Note: Runs 00–12 refer to geometric configurations schematizing the bifurcation-confluence system of the Po River near Gussola, shown in Figure 1. Runs 13–14 correspond to the schematization of another bifurcation-confluence system of the Po River, near Boretto (Reggio Emilia, Italy).

Exner equation governing bed evolution. Each simulation, including that providing the pre-diversion bed topography used as the initial condition for all the others, was run for a time interval large enough (approximately 2 years) to ensure that a quasi-equilibrium configuration is reached in which time variations in the riverbed are minimal.

3 | Results

The framework detailed in the preceding sections enables a comprehensive investigation into the influence of various lateral weir configurations on the equilibrium state of the meander cut-off loop configuration shown in Figure 2. The analysis employs both one-dimensional simplified methods and two-dimensional numerical simulations. While the two-dimensional simulations provide a more nuanced and accurate representation of the governing physical processes, their application is constrained by computational costs. In contrast, the one-dimensional analysis facilitates faster computations, enabling the assessment of equilibrium across a broader range of configurations.

Figure 4 shows the equilibrium profiles of the various main channel reaches resulting from the one-dimensional simulation. Specifically, Figure 4a shows the results of a configuration with a pronounced levee lowering ($\hat{d}=0.5$) and a quite wide secondary channel ($r_c=0.75$), while Figure 4b depicts an higher and narrower side weir ($\hat{d}=0.75$ and $r_c=0.4$). In both cases, lowering the weir enables a portion of the flow to be diverted into the cut-off channel, triggering downstream deposition in the *b*-reach of the main channel. This deposition results from the imbalance between the diverted flow discharge and the diverted sediment discharge. The majority of sediment remains in the main channel, while the diminished flow velocity downstream of the bifurcation reduces sediment transport capacity. The new bed equilibrium is achieved by increasing the local bed slope in the *b*-reach, as well as the free-surface elevation after the lateral diversion. The combined effects of sediment deposition and increased free-surface elevation near the lateral weir enhances flow and sediment diversion into the cut-off channel, as particularly visible in Figure 4a.

Although the one-dimensional framework offers computational efficiency, it oversimplifies the problem near the bifurcation and confluence areas, as well as feedback mechanisms from the cut-off channel. Two-dimensional simulations help to partly overcome these limitations, offering a detailed representation of localized phenomena characteristic of meandering rivers, such as curvature-induced secondary flows and point bar formation.

The same configurations illustrated in Figure 4 were reproduced under the two-dimensional framework (Figure 5). Particularly, the cross-sectionally averaged equilibrium bed profiles along the main channel (Figure 5a,c) and the secondary channel (Figure 5b,d) exhibit morphological patterns consistent with those obtained from the one-dimensional simulations. Sediment deposition invariably prevails in the bend of the main channel included between the bifurcation and the subsequent confluence (*b*-reach in Figure 2a), causing an overall accretion of the bed. This accretion becomes more limited as the weir elevation increases and the secondary channel is narrowed (Figure 5a,b).

Nevertheless, the two-dimensional results also highlight the localized erosion at the side weir and, more importantly, at the confluence. Moreover, differently from the one-dimensional framework, the equilibrium bed topography in the cut-off channel is now resolved. Figure 5b,d show the cross-sectionally averaged equilibrium profiles computed along the cut-off channel. Both the investigated configurations are characterized by strong erosion immediately downstream of the weir, primarily due to flow acceleration in that region. Under subcritical flow conditions, the weir acts as a submerged obstacle (Figure 5b). Conversely, a hydraulic jump forms when the critical flow depth is reached over the weir, due to its elevation increase coupled with the contemporary narrowing of the secondary channel (Figure 5d). In this latter case, the diverted water and sediment discharges reduce to such an extent that they cause the drowning of the end portion of the secondary channel leading to sediment accumulation. As a result, a pronounced bed step develops at the confluence with the main channel, further emphasizing the dominance of the main channel in the bifurcation system.

A general overview of the spatial variations of the equilibrium bed topography obtained with the two-dimensional approach is shown in Figure 6a–c in terms of bed elevation changes relative to the initial flat sloping bed. The results refer to the same equilibrium represented in Figure 5a,b consequent to a levee lowering of approximately half the main channel flow depth ($\hat{d}=0.5$), and a secondary channel width comparable to

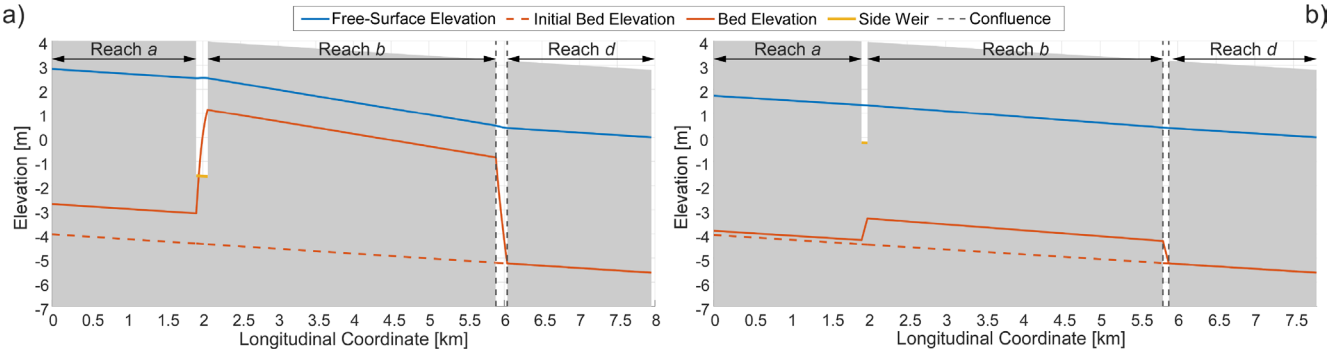

FIGURE 4 | Equilibrium profiles of the various main channel reaches before (dashed lines) and after (continuous lines) cut-off channel re-opening, resulting from the one-dimensional analysis. Parameters for (a) $\hat{d}=0.5$ and $r_c=0.75$, while for (b) $\hat{d}=0.75$ and $r_c=0.40$. The bed profile (orange) is in equilibrium with the free-surface profile (blue). The gray region denotes impermeable levees. The horizontal yellow line represents the side weir elevation after its lowering, while vertical dashed lines indicate the confluence location. [Color figure can be viewed at wileyonlinelibrary.com]

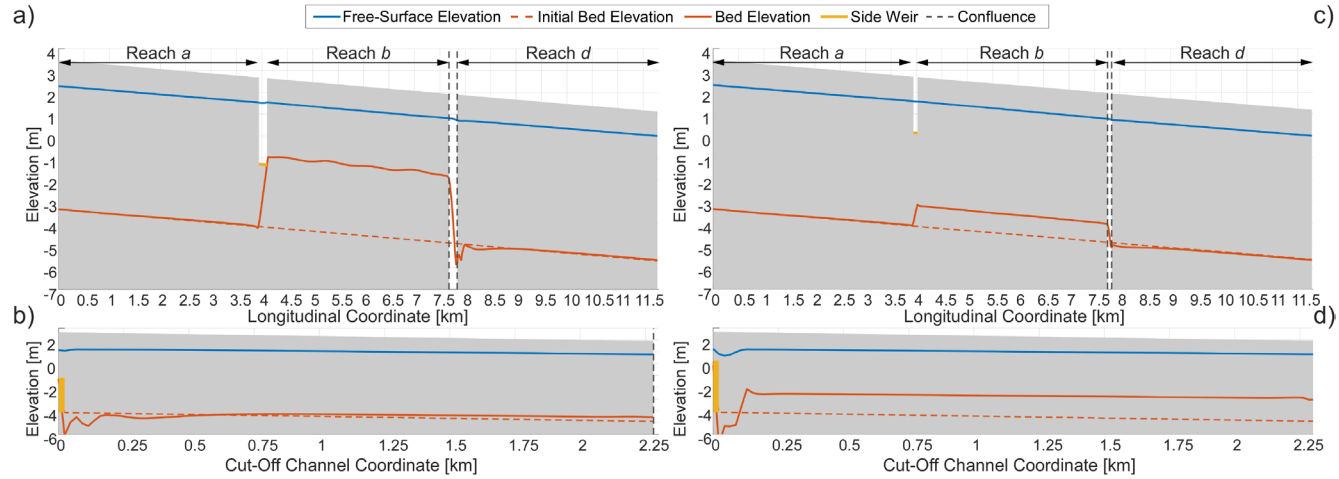

FIGURE 5 | Cross-sectionally averaged longitudinal equilibrium profiles along (a, c) the main channel and (b, d) the secondary channel after cut-off re-opening, computed with the two-dimensional model. Parameters for (a, b) $\widehat{d} = 0.5$ and $r_c = 0.75$ (Run 00), and (c, d) $\widehat{d} = 0.75$ and $r_c = 0.40$ (Run 07). Free-surface and bed profiles are depicted with blue and orange lines, respectively. The gray region denotes impermeable levees. The horizontal yellow line represents the side weir elevation after its lowering, while vertical dashed lines indicate the confluence location. [Color figure can be viewed at wileyonlinelibrary.com]

that of the main channel ($r_c = 0.75$). The opening of the side channel initially induces intense sedimentation in the *b*-reach of the main channel, as the diverted flow reduces the sediment transport capacity of this branch, resulting in sediment accumulation of up to 3 m.

The localized erosion downstream of the side weir is associated with a flow acceleration due to the diversion. In addition, a recirculation cell forms on the inner side of the deflected flow, promoting sediment accumulation (Figure 6b,d). The fixed-bank constraint exacerbates these effects, as natural bank erosion would typically adjust channel curvature. At the confluence, flow re-entry from the secondary channel exhibits higher momentum compared to the approaching flow in the main channel. This causes a deep incision toward the right bank and sediment accumulation along the left bank of the main channel downstream of the confluence (Figure 6c). Recirculation zones with reduced velocities further contribute to localized sediment deposition (Figure 6e). In general, the reduced velocities established in the main channel bend near the confluence, relative to those in the cut-off channel, highlight the increased dominance of this shorter channel. This is in overall agreement with the fixed-bed laboratory experiments by Lin et al. (2025).

The system's evolutionary trends have also been evaluated in terms of average deposition within the branch *b* of the main channel, $\Delta\widehat{\eta}_b$, and the discharge asymmetry, $\Delta\widehat{Q}$, defined as:

$$\Delta\widehat{\eta}_b = \frac{\overline{\eta_b - \eta_{b0}}}{D_a}, \qquad \Delta\widehat{Q} = \frac{Q_b - Q_c}{Q_a}, \tag{22}$$

where $\overline{\eta_b - \eta_{b0}}$ is the average sediment deposition in the branch *b* with respect to the initial configuration (η_{b0}). Note that, as $\Delta\widehat{Q}$ approaches 1, the flow is entirely conveyed through the *b*-reach of the main river course. For $\Delta\widehat{Q} > 0$, this reach remains dominant. Conversely, negative values of $\Delta\widehat{Q}$ indicate that the narrower cut-off channel *c* conveys the majority of the flow. At the extreme of $\Delta\widehat{Q}$ approaching -1, a complete avulsion occurs toward the cut-off channel, leading to intense sedimentation within the *b*-reach of the main river course.

The equilibrium conditions corresponding to each configuration listed in Table 1 are summarized in Figure 7, which shows the dimensionless metrics (22) plotted as a function of the dimensionless inlet parameter, $\widehat{d}$. The one-dimensional modeling results are depicted with continuous lines, while the outcomes of the two-dimensional simulations are represented with colored circles. From Figure 7a, it is evident that the tendency of the secondary cut-off channel to become dominant ($\Delta\widehat{Q} < 0$) are more pronounced as the side weir is progressively lowered (smaller $\widehat{d}$) and widened (larger r_c).

When no flow is diverted into the cut-off channel ($\widehat{d} = 1$), all the discharge continues to flow in the main channel ($\Delta\widehat{Q} = 1$). As $\widehat{d}$ decreases, an increasing portion of the flow is diverted into the secondary channel until, in some cases, the narrower cut-off channel becomes dominant ($\Delta\widehat{Q} < 0$). This trend is observed across all configurations. Increasing the secondary channel width leads to this channel becoming dominant even for quite high values of $\widehat{d}$ (e.g., $\Delta\widehat{Q} < 0$ for $\widehat{d} \approx 0.8$ when $r_c = 0.75$).

The comparison between the discharge asymmetry resulting from the two-dimensional and one-dimensional simulations, although qualitatively similar, exhibits quantitative differences that generally becomes more evident as $\widehat{d}$ decreases, with the one-dimensional model that tends to overestimate the diverted flow discharge. On the other hand, the average deposition in the *b*-reach of the main channel (quantified by $\Delta\widehat{\eta}_b$) resulting from the one-dimensional model increases with the diverted flow discharge, as shown in Figure 7b. In general, two-dimensional results follow the same trend, but with reduced sediment deposition that never exceeds 70% of the upstream flow depth. These differences are related to the higher increase of the free-surface elevation at the side weir in the one-dimensional framework

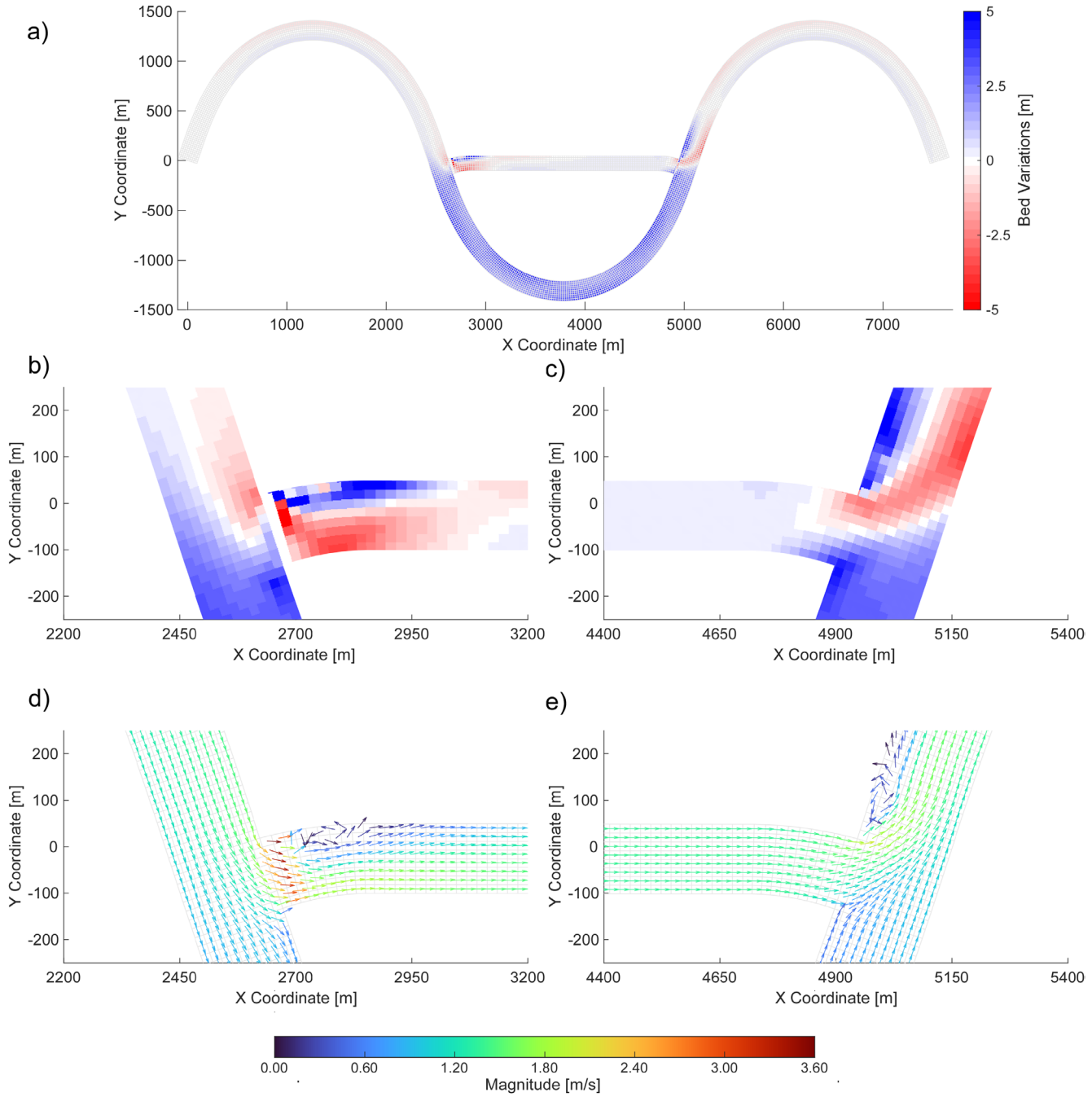

FIGURE 6 | Bed elevation differences at equilibrium after cut-off channel re-opening according to a two-dimensional simulation (Run 00). (a) Bed variations in the schematic meander configuration after side channel re-opening. Panels (b) and (d) show a zoomed view of (b) differences in bed elevation and (d) velocity distribution in the bifurcation area. Panels (c) and (e) shows a zoomed view of (c) differences in bed elevation and (e) velocity distribution in the confluence area. The simulation has been carried out for $\widehat{d} = 0.5, r_c = 0.75$. The Bed Variations colorbar in panel (a) is valid also for panels (b) and (c). The Magnitude colorbar at the bottom of panels (d) and (e) quantifies the velocity magnitude in these panels. [Color figure can be viewed at wileyonlinelibrary.com]

(Figure 4a). Finally, note that even with a quite narrow secondary channel (low r_c) and a relatively high weir elevation (large $\widehat{d}$), which results in a small diverted discharge, some sedimentation still occurs in the main channel ($\Delta\widehat{\eta}_b > 0$, Figure 7b). The bed aggradation caused by this deposition could potentially affect local navigability.

The simulations corresponding to Runs 00–12, have been carried out for a ratio of the secondary to the main channel length $\gamma_L = 0.65$ similar to that observed for a bifurcation-confluence system on the Po River near Gussola (Italy) that has been recently re-naturalized by lowering the side weir separating the main channel from and old cutoff channel. The results indicate that this partial re-opening should invariably produce sedimentation in the main channel bend included between the bifurcation and the subsequent confluence. Indeed, the higher free surface slope that establishes in the secondary channel (slope advantage) triggers a positive feedback mechanism. Erosion in

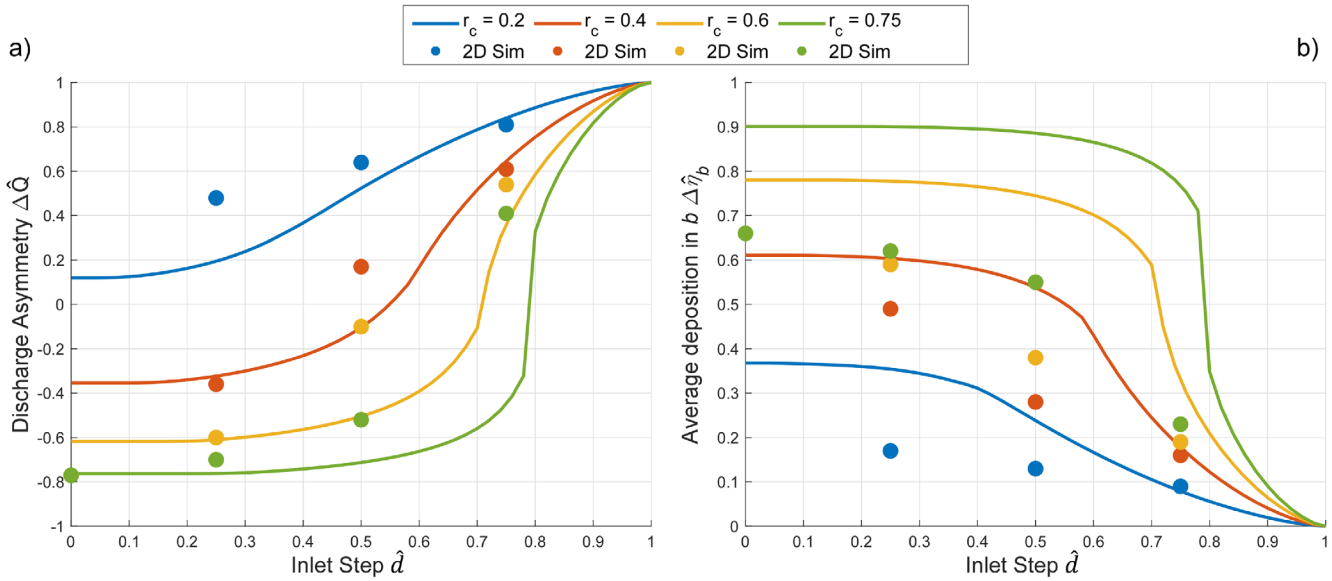

FIGURE 7 | Equilibrium conditions of the system shown in Figure 2, expressed in terms of (a) the discharge asymmetry ($\Delta\widehat{Q}$) and (b) the dimensionless average bed elevation change within the *b*-branch of the main channel ($\Delta\widehat{\eta}_b$), plotted as functions of the inlet step ratio ($\widehat{d}$) for different values of channel branch width ratio (r_c). Continuous lines correspond to the one-dimensional simulation results, while the markers represent outcomes from two-dimensional numerical simulations. [Color figure can be viewed at wileyonlinelibrary.com]

the cut-off channel leads to an increase in the diverted discharge and, consequently, a reduction in the discharge flowing in the *b*-reach of the main channel. This reduction, in turn, produces a decline in sediment transport capacity and, hence, a progressive sediment accumulation in the main channel.

The two-dimensional modeling approach also enables to evaluate the influence of varying branch lengths on the system equilibrium. Accordingly, a configuration characterized by longer and more symmetric branches has been analyzed (specifically, with $\Lambda_b = 0.16$ and $\gamma_L = 0.82$), as illustrated in Figure 8a. This configuration schematizes the conditions characterizing another bifurcation-confluence system, located in a reach of the Po River near Boretto (Reggio Emilia, Italy).

Figure 8 displays the equilibrium condition for this configuration, featuring a levee lowering of approximately half the flow depth in the main channel ($\widehat{d} = 0.5$) and a narrower secondary channel ($r_c = 0.4$). Compared to the more asymmetric configuration shown in Figure 6, the opening of the secondary channel induces minor sedimentation in the *b*-reach of the main channel. This result is due to the less pronounced slope advantage associated with the similar length of the main and secondary channel branches, ultimately leading to a weaker alteration of the main channel bed. In the case of a reduced difference between the length of the main and secondary channel branches, this attenuation of the morphodynamic impact on the main channel bed is evident for all the considered values of the inlet step parameter $\widehat{d}$.

Figure 9 summarizes the equilibrium conditions for configurations with different degree of asymmetry of the main and secondary channel lengths and moderate secondary channel width ($r_c = 0.4$). The comparison highlights how branch length asymmetry influences the bifurcation-confluence system in terms of the dimensionless average bed elevation change in the *b*-reach of the main channel ($\Delta\widehat{\eta}_b$) and dimensionless discharge asymmetry ($\Delta\widehat{Q}$), as defined by relations 22.

In the more symmetric configuration ($\gamma_L = 0.82$), both the diverted discharge and the sedimentation in the *b*-reach are consistently lower for all the inlet step ratios. Interestingly, unlike the more asymmetric case ($\gamma_L = 0.62$), where $\Delta\widehat{\eta}_b$ and $\Delta\widehat{Q}$ display monotonic trends with increasing $\widehat{d}$, the more symmetric configuration exhibits a non-monotonic response. Specifically, the configuration with $\widehat{d} = 0.25$ results in the least alteration of the original bed of the *b*-reach. In this scenario, the cut-off channel receives more sediment than it can transport, leading to significant bed aggradation. The deposited sediment ultimately submerges the side weir, maintaining a residual water depth of approximately 2 m.

4 | Discussion

Recent re-naturalization proposals have focused on partially restoring the natural viability of rivers by re-opening former secondary channels. However, these interventions inevitably alter river equilibrium, potentially triggering undesirable morphodynamic responses. In particular, the re-establishment of morphological configurations involving bifurcation–confluence loops has been associated with deposition processes, as extensively documented in the literature (Ragno et al. 2021; Durante et al. 2024).

A distinct feature of the current study is the control of the upstream bifurcation through an artificial weir. The presence of this weir is not accounted for in the standard assumptions of classical bifurcation theories, rendering them inapplicable. An alternative model framework is thus introduced in this study to address the equilibrium conditions of these bifurcation-loop configurations often encountered in engineering practice

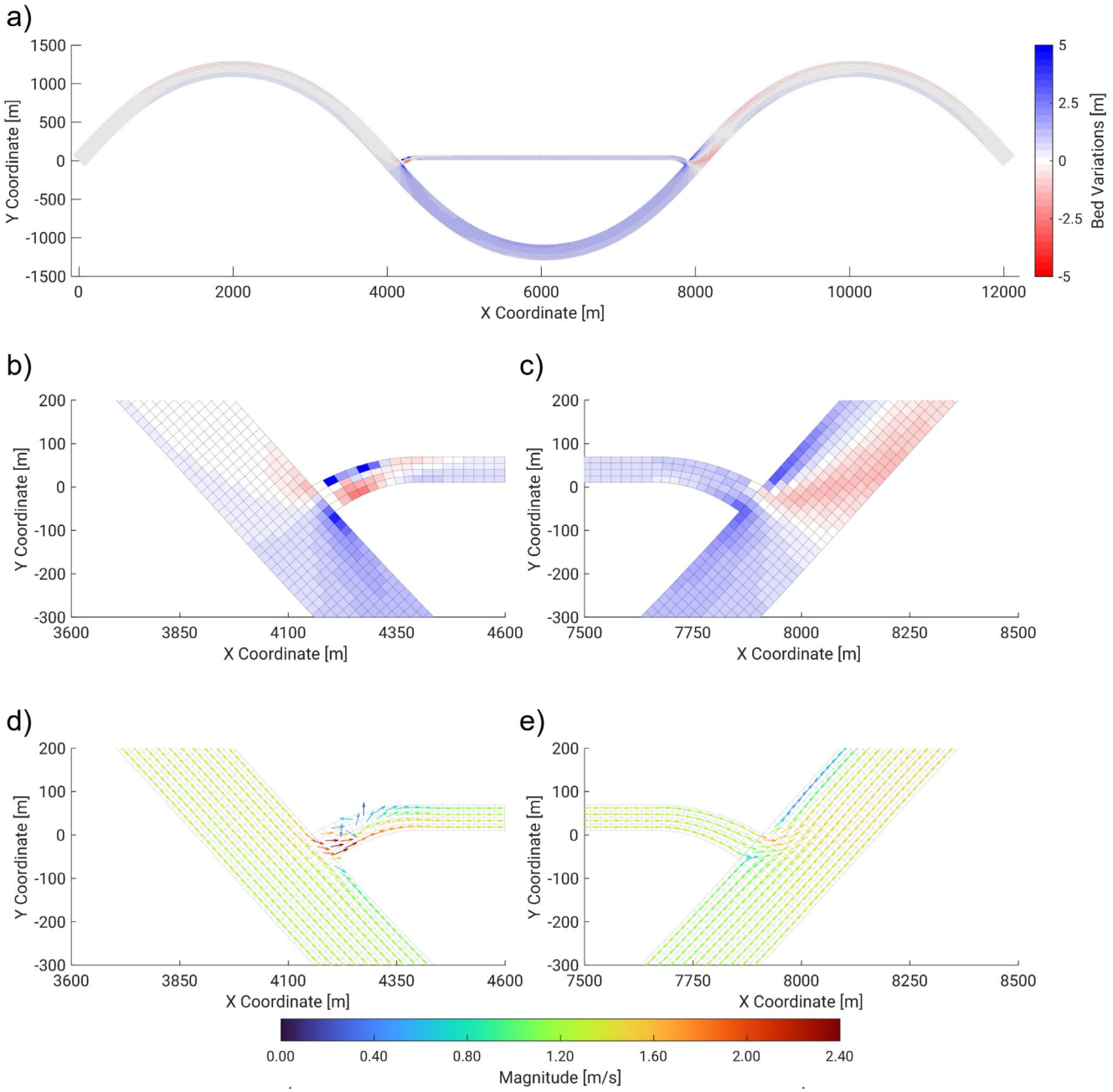

FIGURE 8 | Bed elevation differences at equilibrium after cut-off channel re-opening according to a two-dimensional simulation (Run 14). (a) Bed variations in the schematic meander configuration after side channel re-opening. Panels (b) and (d) show a zoomed view of (b) differences in bed elevation and (d) velocity distribution in the bifurcation area. Panels (c) and (e) shows a zoomed view of (c) differences in bed elevation and (e) velocity distribution in the confluence area. The simulation has been carried out for $\widehat{d} = 0.5$, $r_c = 0.4$, $\Lambda_b = 0.16$, and $\gamma_L = 0.82$. The Bed Variations colorbar in panel (a) is valid also for panels (b) and (c). The Magnitude colorbar at the bottom of panels (d) and (e) quantifies the velocity magnitude in these panels. [Color figure can be viewed at wileyonlinelibrary.com]

(Figure 1). The proposed approach allows for a systematic exploration of the effects of various lateral weir configurations on the morphodynamic equilibrium of a simplified meander cut-off loop, mimicking the geometry of real cut-off re-openings already carried out or planned on the Po River.

The one-dimensional approach presented in Section 2.2 allows for quick simulations, letting to explore rapidly the parameter space and, hence, determine equilibrium conditions across a broad spectrum of configurations. Key trends in the flow partitioning ($\Delta\widehat{Q}$) at the upstream bifurcation can then be identified, depending on two relevant dimensionless parameters. The first, $\widehat{d}$, quantifies the elevation of the side weir used to control the diverted flow compared to the flow depth in the main channel, while the second, r_c, accounts for the secondary channel width compared to that of the main channel. A reduction in $\widehat{d}$ results in a larger portion of the flow being diverted into the narrower cut-off channel. Similarly, an increase in r_c leads to enhanced flow diversion, thereby amplifying the tendency of dominate of the cut-off channel (Figure 7).

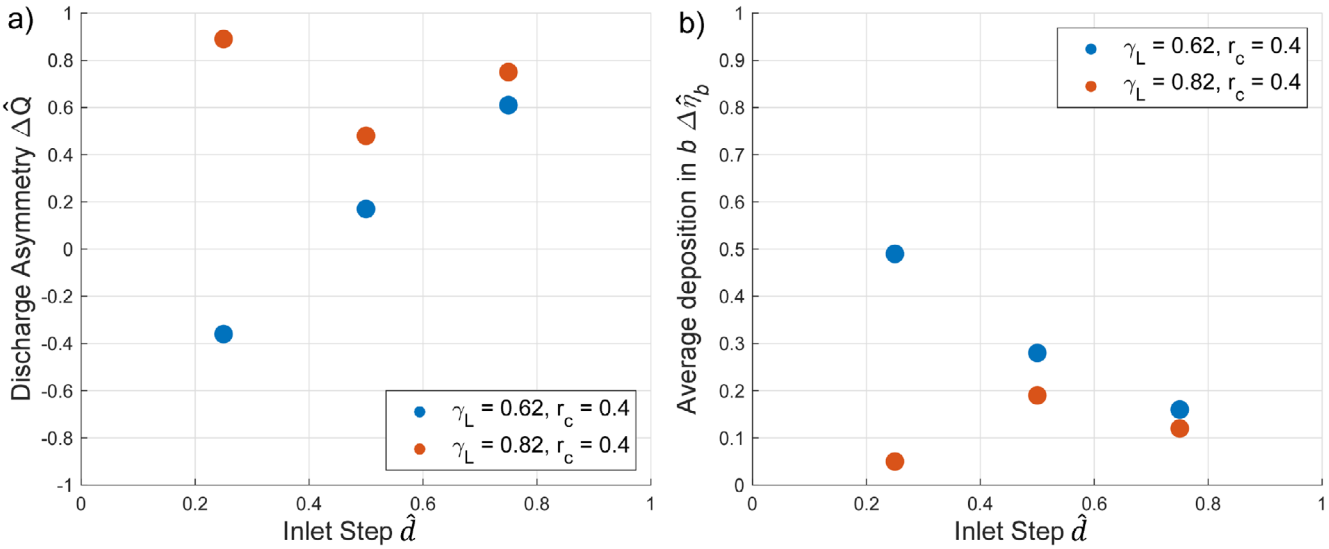

FIGURE 9 | Equilibrium conditions of bifurcation-confluence systems with different degree of asymmetry in the branch lengths according to two-dimensional simulations. The results are expressed in terms of (a) the dimensionless discharge asymmetry ($\Delta\hat{Q}$) and (b) the dimensionless average bed elevation change in the *b*-branch of the main channel ($\Delta\hat{\eta}_b$), plotted as functions of the inlet step ratio ($\hat{d}$). Blue markers represent the more asymmetric configuration ($\gamma_L = 0.62$, $\Lambda_b = 0.13$, and $r_c = 0.4$), while orange markers represent the less asymmetric one ($\gamma_L = 0.82$, $\Lambda_b = 0.16$, and $r_c = 0.4$). [Color figure can be viewed at wileyonlinelibrary.com]

Unlike classical bifurcation models based on a two-cell treatment of sediment partition at the bifurcation (e.g., Bolla Pittaluga et al. 2003), in the present study flow discharge asymmetry is not mirrored by a corresponding sediment discharge asymmetry. This is essentially due to the impediment posed by the side weir in diverting bedload and suspended sediment into the secondary channel. Consequently, the equilibrium in the main channel is reached by increasing the bed slope in the reach included between the bifurcation and the subsequent confluence. This slope increment allows the main channel to accommodate the surplus of sediment within it to compensate for the reduced transport capacity caused by the diversion of part of the water discharge. This adjustment, in turn, elevates the free-surface level at the bifurcation, further intensifying flow diversion into the cut-off channel. As a result, the diverted discharge deviates significantly from predictions based on either fixed bed conditions, as observed in laboratory experiments (Paris et al. 2012; Lin et al. 2025), or two-cell bifurcation models.

The present analysis has been conducted considering a uniform fine sand, a sediment typical of the Po river reaches that have been, or are planned to be, subject to secondary channels reopening. In this context the total load predictor of Engelund and Hansen (1967) and the Rouse sediment concentration profiles provide reliable estimates of the intensity of sediment transport in the main and secondary channels, and on the amount of sediment overpassing the side weir. Nevertheless, in the presence of a sediment mixture containing a non-negligible fraction of coarse sediment the bedload can hardly overcome the weir. Consequently, a lower portion of total load is capable of being diverted by the weir, thus exacerbating the morphodynamic effects determined by a surplus of sediment in the main channel as compared to a decreased transport capacity.

The one-dimensional model inevitably embeds some limitations due to its inherent simplifications. First of all, it treat the secondary channel simply as a water and sediment bypass and, hence, it does not describe the feedbacks between the secondary channel bed morphology and the main channel bed equilibrium. Explicitly modeling the cut-off channel morphodynamic equilibrium would impose a constraint on the free-surface elevation at the side weir, eventually resulting in a lower free surface on the weir. This lowering, in turn, limits the increase in water surface slope within the *b*-reach of the main channel as a mechanism to accommodate the surplus of sediment due to the diversion. Additionally, the upstream portion of the cut-off channel might drown, thereby possibly invalidating the assumption of a constant lateral discharge coefficient used to compute the diverted discharge. This underscores the need for further studies aimed at refining the estimation of this coefficient across a range of morphologies and configurations, in order to fully capture the feedback mechanisms within a one-dimensional modeling framework.

Even though the one-dimensional model effectively reproduces the overarching trends of the investigated system, providing reliable preliminary insights, its simplified nature precludes consideration of the analysis of localized patterns which are commonly observed at both bifurcations and confluences (Paris et al. 2012; Kästner and Hoitink 2020; De Ruijsscher et al. 2020; Ragno et al. 2021; Lin et al. 2025). To address these aspects, two-dimensional, depth-averaged numerical simulations, incorporating curvature-induced secondary flows, have been conducted. In general, two-dimensional simulations offer a more detailed representation of flow partitioning at the bifurcation, capturing feedback effects associated with the flow and sediment distribution in the cut-off channel.

In particular, the two-dimensional modeling framework allows for the incorporation of planform geometry effects on the system equilibrium. Beyond the width of the cut-off channel, the relative lengths of the bifurcating branches play a critical

role in determining this equilibrium (Salter et al. 2018; Redolfi et al. 2019; Ragno et al. 2021; Barile et al. 2023; Durante et al. 2024). Theoretical models have shown the existence of threshold conditions beyond which the system consistently evolves toward a configuration dominated by the shorter branch (Durante 2025). However, in the case examined here, the equilibrium outcome is non-trivial due to the presence of a side weir that controls the inflow into the secondary, shorter branch.

Results of present two-dimensional simulations show that, even in the presence of a side weir, bifurcation-confluence loop systems with highly asymmetrical branch lengths (e.g., $\gamma_L = 0.62$) will ultimately experience avulsion toward the shorter path, although delayed, due to the slope advantage in the shorter branch. In contrast, configurations with more moderate asymmetry (e.g., $\gamma_L = 0.82$) do not exhibit a clear monotonic trend with decreasing weir height, $\widehat{d}$. This behavior arises from the combined influence of sediment diversion at the upstream bifurcation and the comparatively lower momentum of the cut-off channel flow entering in the main channel at the confluence, which promotes sediment deposition in the secondary channel.

Both the one-dimensional and the two-dimensional results indicate minimal overall morphological variations in the main channel reach downstream of the confluence, except for local erosion at the point of reconnection. This outcome is not unexpected, as the total discharge recovers its un-diverted value due to continuity constraints, consistent with the constant discharge requirement imposed at the downstream boundary. Nevertheless, in natural settings, both the channel planform and the bed topography outside of the main channel reach included between the bifurcation and the confluence can affect the morphodynamic equilibrium of adjacent meander bends, depending on the sub- super-resonant character of the morphodynamic regime (Zolezzi and Seminara 2001). Some insights can be drawn from observations of natural bend cut-offs in meandering rivers, where the initial slope advantage provided by the shorter path is eventually equilibrated across the reaches upstream and downstream of the considered meander as the new equilibrium is reached (Viero et al. 2018; Van Denderen et al. 2018).

The present findings highlight the morphological processes induced by the re-opening of a cut-off channel. Notably, deposition in the main channel is observed even under relatively modest diverted discharges. This depositional tendency can also be interpreted with reference to the main channel–cutoff system as a whole. The reactivation of the secondary channel can be conceptualized as a virtual overall widening of the main channel section, where deposition takes place due to a reduction in main velocity and, hence, a decrease in transport capacity.

Nevertheless, the investigated intervention leading to an increased diverted flow unequivocally reactivates fluvial processes, including bedload transport and bank erosion. Furthermore, this phenomenon may promote the rejuvenation of both aquatic and riparian habitats along the floodplain, thereby contributing to the formation of thermal refuge areas during the summer period (Eschbach et al. 2018; Chardon et al. 2025).

5 | Conclusions

This study has explored the complex interplay of hydrodynamic, sediment transport, and morphological processes associated with the re-opening of secondary channels in meandering rivers forming a bifurcation–confluence looping system. While such interventions hold promise for restoring natural flow dynamics and ecological functions, they also induce significant alterations in flow and sediment dynamics, necessitating thorough evaluation to prevent unintended alterations of the main river.

These re-opening projects can be conceptualized as localized upstream lateral diversions and downstream rejoining of flow and sediment. The bed equilibrium of these bifurcation-confluence loops has been first analyzed using a one-dimensional approach. The sediment deposition expected in the main channel has been evaluated by calculating the diversion of flow and sediment at the secondary channel inlet, and reintegrating them at the downstream confluence of the main and secondary channels. As expected, wider secondary channels (larger r_c) and lower side weir elevations (smaller $\widehat{d}$) result in increased discharge diversion and, consequently, more pronounced sediment deposition in the main channel reach located between the bifurcation and the confluence.

These outcomes have been subsequently validated through two-dimensional (i.e., depth-averaged) numerical simulations, which provided a more comprehensive understanding of the localized mechanisms governing lateral diversion and confluence dynamics. However, these simulations also underscored the critical influence of main and secondary branch lengths in determining nontrivial equilibrium configurations.

Overall, the present findings indicate that re-activating old cut-off channels invariably induces sediment deposition in the main channel due to the reduced sediment transport capacity resulting from the diversion. Configurations with wider secondary channel (i.e., larger width ratio r_c) and lower weir elevations (i.e., smaller $\widehat{d}$) exhibit the most significant depositional impacts, highlighting the need of a trade-off between restoring flow connectivity and mitigating sedimentation in the main channel, which could influence local navigability, as well as bank stability.

Finally, even in the presence of a side weir, bifurcation-confluence loop systems with highly asymmetrical branch lengths can ultimately experience avulsion toward the shorter path, although delayed, due to the slope advantage in the shorter branch. In contrast, configurations with relatively moderate asymmetry do not exhibit a clear monotonic trend with decreasing weir height.

Acknowledgments

The authors have nothing to report.

Disclosure

The authors have nothing to report.

Conflicts of Interest

The authors declare no conflicts of interest.

Data Availability Statement

The data that support the findings of this study are available from the corresponding author upon reasonable request.

References

Arthington, Á. H., R. J. Naiman, M. E. Mcclain, and C. Nilsson. 2010. "Preserving the Biodiversity and Ecological Services of Rivers: New Challenges and Research Opportunities." *Freshwater Biology* 55, no. 1: 1–16.

Barile, G., M. Redolfi, and M. Tubino. 2023. "Analysis of Autogenic Bifurcation Processes Resulting in River Avulsion." *EGUsphere* 2023: 1–26.

Bolla Pittaluga, M., G. Coco, and M. G. Kleinhans. 2015. "A Unified Framework for Stability of Channel Bifurcations in Gravel and Sand Fluvial Systems." *Geophysical Research Letters* 42, no. 18: 7521–7536.

Bolla Pittaluga, M., R. Repetto, and M. Tubino. 2003. "Channel Bifurcation in Braided Rivers: Equilibrium Configurations and Stability." *Water Resources Research* 39, no. 3: 1046. https://doi.org/10.1029/2001WR001112.

Bolla Pittaluga, M., and G. Seminara. 2003. "Depth Integrated Modeling of Suspended Sediment Transport." *Water Resources Research* 39, no. 5: 1137. https://doi.org/10.1029/2002WR001306.

Chardon, V., G. Skupinski, and L. Schmitt. 2025. "Assessing the Impacts of Regulation Works on an Upper Rhine Reach for Developing a Process-Based Restoration Framework." *Geomorphology* 478: 109731. https://doi.org/10.1016/j.geomorph.2025.109731.

Collas, F. P. L., A. D. Buijse, L. Van den Heuvel, et al. 2018. "Longitudinal Training Dams Mitigate Effects of Shipping on Environmental Conditions and Fish Density in the Littoral Zones of the River Rhine." *Science of the Total Environment* 619: 1183–1193.

De Marchi, G. 1934. "Saggio di Teoria del Funzionamento Degli Stramazzi Laterali (Theoretical Knowledge on the Functioning of Sideweirs)." *L'energia Elettria* 11, no. 11: 849–860.

De Ruijsscher, T., B. Vermeulen, and A. Hoitink. 2020. "Diversion of Flow and Sediment Toward a Side Channel Separated From a River by a Longitudinal Training Dam." *Water Resources Research* 56, no. 6: e2019WR026750.

Doriano, C., and P. Sandra. 1995. Channel Changes on the Po River, Mantova Province, Northern Italy.

Durante, L. 2025. "Modelling From Single River Bifurcations to Complex Deltas and Comparison With Field Observations". PhD Thesis at the University of Genoa. https://hdl.handle.net/20.500.14242/218362.

Durante, L., M. Bolla Pittaluga, G. Porcile, and N. Tambroni. 2024. "Downstream Control on the Stability of River Bifurcations." *Journal of Geophysical Research: Earth Surface* 129: e2023JF007548. https://doi.org/10.1029/2023JF007548.

Engelund, F., and E. Hansen. 1967. *A Monograph on Sediment Transport*. Technisk Forlag.

Eschbach, D., L. Schmitt, G. Imfeld, et al. 2018. "Long-Term Temporal Trajectories to Enhance Restoration Efficiency and Sustainability on Large Rivers: An Interdisciplinary Study." *Hydrology and Earth System Sciences* 22, no. 5: 2717–2737. https://doi.org/10.5194/hess-22-2717-2018.

European Commission. 2023. Eu Biodiversity Strategy for 2030. https://environment.ec.europa.eu/strategy/biodiversity-strategy-2030_en.

Formann, E., H. Habersack, H. M. Habersack, and S. Schober. 2007. "Morphodynamic River Processes and Techniques for Assessment of Channel Evolution in Alpine Gravel Bed Rivers." *Geomorphology* 90, no. 3–4: 340–355.

Habersack, H., and H. Piégay. 2007. "River Restoration in the Alps and Their Surroundings: Past Experience and Future Challenges." *Developments in Earth Surface Processes* 11: 703–735. https://doi.org/10.1016/S0928-2025(07)11161-5.

Ikeda, S., G. Parker, and K. Sawai. 1981. "Bend Theory of River Meanders. Part 1. Linear Development." *Journal of Fluid Mechanics* 112: 363–377.

Kästner, K., and A. Hoitink. 2020. "Idealized Model for the Deflection of Sediment Into Lateral Branches of Lowland Rivers." *Water Resources Research* 56, no. 6: e2019WR026602.

Lanzoni, S., R. Luchi, and M. Bolla Pittaluga. 2015. "Modeling the Morphodynamic Equilibrium of an Intermediate Reach of the Po River (Italy)." *Advances in Water Resources* 81: 95–102. https://doi.org/10.1016/j.advwatres.2014.11.004.

Le, T., A. Crosato, and W. Uijttewaal. 2018. "Long-Term Morphological Developments of River Channels Separated by a Longitudinal Training Wall." *Advances in Water Resources* 113: 73–85.

Leopold, L. B., M. G. Wolman, and J. P. Miller. 1964. *Fluvial Processes in Geomorphology*. Freeman.

Lin, J. T. Y., E. Lacunza, R. Fernández, et al. 2025. "Hydrodynamic Processes of Incipient Meander Chute Cutoffs: Laboratory Experiments With Implications for Morphodynamics and Depth-Averaged Modeling." *Water Resources Research* 61, no. 3: e2024WR038502.

Malmqvist, B., and S. Rundle. 2002. "Threats to the Running Water Ecosystems of the World." *Environmental Conservation* 29, no. 2: 134–153.

Marchetti, M. 2002. "Environmental Changes in the Central Po Plain (Northern Italy) due to Fluvial Modifications and Anthropogenic Activities." *Geomorphology* 44, no. 3–4: 361–373.

Michelazzo, G., L. Minatti, E. Paris, and L. Solari. 2016. "Side Weir Flow on a Movable Bed." *Journal of Hydraulic Engineering* 142, no. 6: 04016007.

Paris, E., L. Solari, and G. Bechi. 2012. "Applicability of the de Marchi Hypothesis for Side Weir Flow in the Case of Movable Beds." *Journal of Hydraulic Engineering* 138, no. 7: 653–656.

Poppe, M., J. Kail, J. Aroviita, M. Stelmaszczyk, M. Giełczewski, and S. Muhar. 2016. "Assessing Restoration Effects on Hydromorphology in European Mid-Sized Rivers by Key Hydromorphological Parameters." *Hydrobiologia* 769: 21–40.

Ragno, N., M. Redolfi, and M. Tubino. 2021. "Coupled Morphodynamics of River Bifurcations and Confluences." *Water Resources Research* 57, no. 1: e2020WR028515.

Redolfi, M., G. Zolezzi, and M. Tubino. 2019. "Free and Forced Morphodynamics of River Bifurcations." *Earth Surface Processes and Landforms* 44, no. 4: 973–987.

Rinaldi, M. 2021. "Bed-Level Adjustements in the Po River Catchment (Northern Italy)." *Italian Journal of Engineering Geology and Environment* 2: 41–50.

Rinaldi, M., N. Surian, F. Comiti, and M. Bussettini. 2013. "A Method for the Assessment and Analysis of the Hydromorphological Condition of Italian Streams: The Morphological Quality Index (mqi)." *Geomorphology* 180: 96–108.

Salter, G., C. Paola, and V. R. Voller. 2018. "Control of Delta Avulsion by Downstream Sediment Sinks." *Journal of Geophysical Research: Earth Surface* 123, no. 1: 142–166.

Seminara, G., S. Lanzoni, and N. Tambroni. 2024. *Theoretical Morphodynamics: Straight Channels*. Firenze University Press.

Simons, J. H., C. Bakker, M. H. Schropp, L. H. Jans, F. R. Kok, and R. E. Grift. 2001. "Man-Made Secondary Channels Along the River Rhine

(The Netherlands); Results of Post-Project Monitoring." *Regulated Rivers: Research & Management* 17, no. 4–5: 473–491.

Slingerland, R., and N. D. Smith. 1998. "Necessary Conditions for a Meandering River Avulsion." *Geology* 26, no. 5: 435–438.

Surian, N., L. Ziliani, F. Comiti, M. A. Lenzi, and L. Mao. 2009. "Channel Adjustments and Alteration of Sediment Fluxes in Gravel-Bed Rivers of North-Eastern Italy: Potentials and Limitations for Channel Recovery." *River Research and Applications* 25, no. 5: 551–567.

Van Denderen, R. P., R. M. Schielen, A. Blom, S. J. Hulscher, and M. G. Kleinhans. 2018. "Morphodynamic Assessment of Side Channel Systems Using a Simple One-Dimensional Bifurcation Model and a Comparison With Aerial Images." *Earth Surface Processes and Landforms* 43, no. 6: 1169–1182.

Vaughn, C. C. 2010. "Biodiversity Losses and Ecosystem Function in Freshwaters: Emerging Conclusions and Research Directions." *Bioscience* 60, no. 1: 25–35.

Viero, D. P., S. L. Dubon, and S. Lanzoni. 2018. "Chute Cutoffs in Meandering Rivers: Formative Mechanisms and Hydrodynamic Forcing." *Fluvial Meanders and Their Sedimentary Products in the Rock Record*, 201–229. https://doi.org/10.1002/9781119424437.ch8.

Zolezzi, G., and G. Seminara. 2001. "Downstream and Upstream Influence in River Meandering. Part 1. General Theory and Application to Overdeepening." *Journal of Fluid Mechanics* 438, no. 13: 183–211.